Resonant Tunneling Diode Nano-Optoelectronic Excitable Nodes for Neuromorphic Spike-Based Information Processing

Matěj Hejda,[1,*] Juan Arturo Alanis,[1] Ignacio Ortega-Piwonka,[2] João Lourenço,[3] José Figueiredo,[3] Julien Javaloyes,[2] Bruno Romeira,[4] and Antonio Hurtado[1]

[1] *Institute of Photonics, SUPA Dept of Physics, University of Strathclyde, Glasgow G11RD, United Kingdom*

[2] *Dept de Física and IAC-3, Universitat de les Illes Balears, Palma de Mallorca 07122, Spain*

[3] *Centra-Ciências and Departamento de Física, Faculdade de Ciências, Universidade de Lisboa, Lisboa 1749-016, Portugal*

[4] *Ultrafast Bio and Nanophotonics Group, International Iberian Nanotechnology Laboratory, Braga 4715-330, Portugal*

(Received 22 July 2021; revised 14 January 2022; accepted 26 January 2022; published 25 February 2022)

In this work, we introduce an interconnected nano-optoelectronic spiking artificial neuron emitter-receiver system capable of operating at ultrafast rates (about 100 ps/optical spike) and with low-energy consumption (< pJ/spike). The proposed system combines an excitable resonant tunneling diode (RTD) element exhibiting negative differential conductance, coupled to a nanoscale light source (forming a master node) or a photodetector (forming a receiver node). We study numerically the spiking dynamical responses and information propagation functionality of an interconnected master-receiver RTD node system. Using the key functionality of pulse thresholding and integration, we utilize a single node to classify sequential pulse patterns and perform convolutional functionality for image feature (edge) recognition. We also demonstrate an optically interconnected spiking neural network model for processing of spatiotemporal data at over 10 Gbit/s with high inference accuracy. Finally, we demonstrate an off-chip supervised learning approach utilizing spike-timing-dependent plasticity for the RTD-enabled photonic spiking neural network. These results demonstrate the potential and viability of RTD spiking nodes for low footprint, low-energy, high-speed optoelectronic realization of spike-based neuromorphic hardware.

DOI: 10.1103/PhysRevApplied.17.024072

I. INTRODUCTION

With the magnitude of data production increasing exponentially, machine learning (ML) approaches and the field of artificial intelligence (AI) have been undergoing a booming development, rapidly becoming ubiquitous in all domains of human endeavor. These methods have allowed machines to gain humanlike information processing capabilities [e.g., learning, computer vision, natural language processing (NLP), or complex pattern recognition] and to solve significant computational problems [1]. While AI algorithms achieve breakthroughs, the hardware used to run those receives in turn less attention. Nowadays, large-scale ML models are typically trained on cloud-based computing clusters, with some estimates placing the training energy consumption for a state-of-the-art NLP model on par with six years of total power energy consumption of a human brain [2]. Driven by the goal of reducing energy consumption as well as by the plateauing of empirical chip scaling laws, there has recently been significant growth of interest in nonconventional computing approaches. Neuromorphic (brainlike) engineering develops computer hardware architectures inspired by the brain and by the behavior of biological neurons. Neuromorphic systems can be operated at various degrees of biological plausibility, directly mapping conventional artificial neural network algorithms onto hardware or capitalizing on the rich dynamical behavior of biological neurons for information processing. While there already are powerful neuromorphic systems based on electronics [3,4], the reliance on CMOS technology imposes limits in terms of interconnectivity and component density, with dozens of transistors required per neuron and additional external memories needed for synaptic weights. This results in several micrometer large neurons. Since dedicated wiring for every synaptic link is not practical, neuromorphic electronic systems usually employ a shared digital communication bus with time-division multiplexing [5], gaining interconnectivity at the expense of bandwidth, or use schemes such as address-event representation [6]. As an alternative, hardware technologies relying on physics for neuromorphic computation are nowadays

*matej.hejda@strath.ac.uk

gaining increasing research interest. These include hybrid CMOS-memristive systems (see Ref. [2] for an overview), spintronics [7], and photonic systems [8,9].

Neuromorphic photonics is a nascent field, recently gaining significant traction due to increasing importance of AI algorithms and rapid advances in the field of photonic integrated circuits. Optoelectronic systems in particular are considered as highly suitable for future cognitive computing hardware, as they benefit from operation with both electrons and photons, each excelling at different key functionalities [10]. Thanks to their capability to address bandwidth and interconnect energy limits in a scalable fashion, optoelectronic systems might prove to be the optimal solution to overcome these limitations [11]. There are many different approaches to realization of artificial neural networks in optics (see, for example, Ref. [12]). Using delayed feedback, recurrent neural networks can be realized in a photonic reservoir computer, yielding networks with a large number of virtual nodes while only requiring very low hardware complexity [13]. Closer to the usual digital implementation of artificial neural networks are platforms that enable accelerated matrix (tensor) based computation [14,15]. Some photonic systems, such as diffractive surfaces [16,17], may allow for passive computation by interaction between light and matter. One of the key principles when designing biologically plausible neuromorphic hardware is excitability and event-based signaling. Biological neurons communicate with electronic signals using a sparse encoding scheme known as *spiking*. Photonic spike-based neuromorphic systems include phase-change material-based integrated networks of microring resonators [18,19], photonic crystals [20], superconducting Josephson junctions [21], micropillar lasers [22], excitable semiconductor lasers, including a graphene laser with saturable absorber [23], quantum-dot laser [24–26], microring resonators [27], vertical cavity surface emitting lasers (VCSELs) [28–30], and multisection VCSELs with saturable absorber [31,32]. Table I provides a comparison of some of these approaches. This wide array of investigated technologies demonstrates the power and high potential of photonics for unconventional brain-inspired computing. Despite the impressive progress, the development of a single, miniaturized light-emitting nanoscale source and detector for spike-based operation (which is key for spike-based, neuromorphic computing in the optoelectronic domain) remains an ongoing, significant challenge.

II. SPIKING NEUROMORPHIC RTD-POWERED OPTOELECTRONIC NODES

In this work, we introduce an optoelectronic spike-based neuromorphic system utilizing a resonant tunneling diode (RTD) element based on a double barrier quantum well (DBQW) epilayer structure. The DBQW consists of a narrow bandgap semiconductor layer embedded between two thin layers with a wider bandgap [Fig. 1(d), inset], with typical barrier thicknesses ranging from 4 to 8 nm, and 1 to 3 nm, respectively. Under applied voltage, the structure works as a filter for the carrier's energy, leading to high carriers' transmission when the energy of the electrons (Fermi sea) resonates with the confinement energy levels of the DBQW. The voltage-controlled probability for incident electrons to cross the barrier is locally maximized, which results in the typical N-shaped voltage-current relation $f(V)$ with one or more regions of negative differential conductance (NDC) in between two or more regions of positive differential conductance (PDC) [36], as shown in Fig. 1(d). The presence of the nonlinearity and gain in the NDC region, persisting up to terahertz frequencies [37], makes RTDs particularly suitable for high-frequency oscillators [38]. This nonlinearity is key for operation of the proposed spiking neuromorphic RTD node as a fast, excitable spiking nonlinear source [39] with intrinsic electrical gain. Previous works have investigated triggering of stochastic excitable responses in hybrid integrated optoelectronic RTD circuits [40,41] and operation of RTDs with delayed feedback [42], addressing only operation of a single (solitary) device. In this work, we investigate interconnected systems consisting of multiple independent RTD-based monolithic integrated optoelectronic nodes. We employ the nodes as stateless excitable devices and take advantage of the spike-based signaling to implement information processing tasks and multidevice networks with prospects for very low footprint, low-energy, and high-speed operation due to the use of sub-λ elements. We utilize two types of nodes: an electronic-optical (E-O) RTD-LD system, realized with a RTD element coupled

TABLE I. Comparison of photonic and optoelectronic technologies capable of spike- (pulse) based signaling.

Photonic platform	Energy per event (J)	Spike event timescales
Superconducting Josephson junctions (cryogenic) [21]	$> 2 \times 10^{-14}$	> 1 ns (nTron switching)
Phase-change material cells [18]	$\sim 10^{-12}$	$\sim$ 500 ps–1.5 ns (read & write)
Micropillars [33]	$\sim 5 \times 10^{-14}$ (excl. pump)	$\sim$ 200 ps
Graphene laser with saturable absorber [34]	$\sim 10^{-8}$	$\sim 20\ \mu$s
RTD optoelectronic node (this work)	$\sim 10^{-13}$	$\sim$ 100 ps

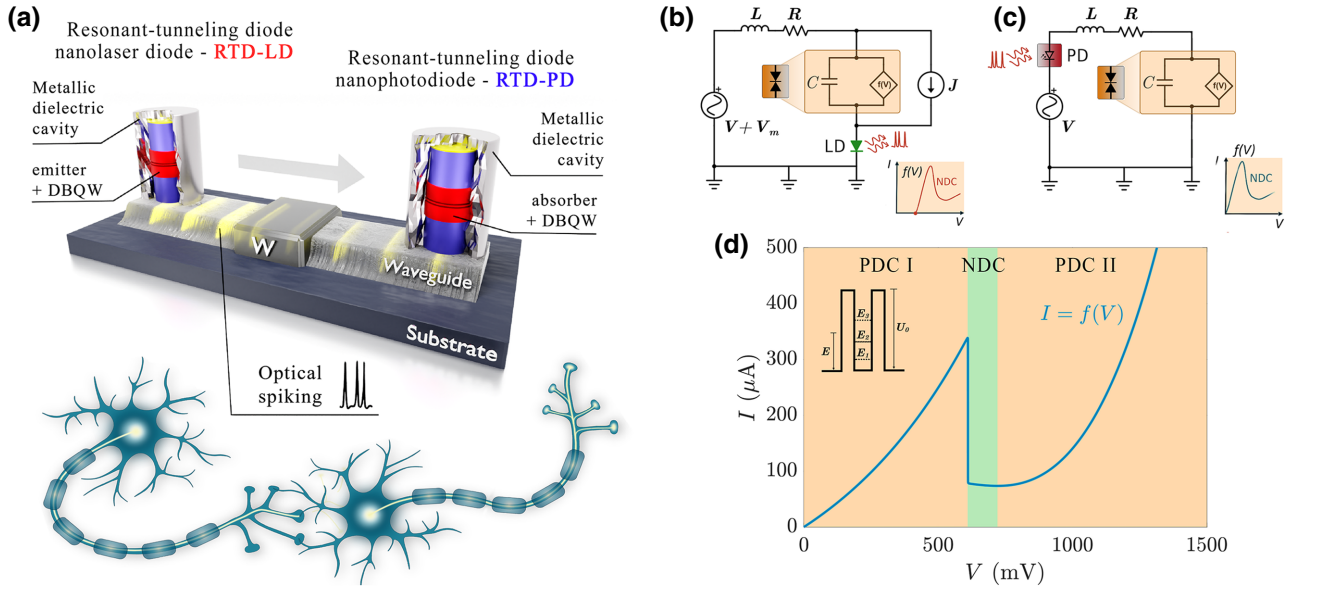

FIG. 1. (a) Illustration of the proposed solution for a spike-based neuromorphic system based on two types of RTD-powered optoelectronic nodes: RTD-LD (master) and RTD-PD (receiver) nodes. The RTD-LD and RTD-PD metal-dielectric encapsulated micropillars are coupled using a waveguide with adjustable attenuation factor W. When subject to external bias, RTD-LD nodes can respond to incoming perturbations with short optical pulses (spikes), which can be processed in the downstream RTD-PD node. This functionality mimics the use of an action potential in biological neurons. (b) Lumped circuit scheme for the RTD-LD node. (c) Lumped circuit diagram from the RTD-PD node. (d) The RTD I-V characteristic used in this study, with curve parameters obtained by fitting experimental data (see the Supplemental Material [35] for the parameters). Regions of positive differential conductance (PDC) and negative differential conductance (NDC) are highlighted in different colors. The inset shows a simplified DBQW scheme with the discrete energy levels inside the well. Typical thickness of the DBQW region is around 10 nm.

to a nanoscale laser diode (LD), and an optical-electronic (O-E) RTD-PD system, realized with a photodiode (PD) coupled to a RTD element. In both node types, the spiking threshold can be adjusted via bias voltage tuning. An illustration of two nodes with an unidirectional optical weighted link, representing two feedfoward linked neurons, is depicted in Fig. 1(a).

A. Optoelectronic RTD-system architecture

In both the RTD-LD and RTD-PD nodes, the two functional blocks are integrated in a monolithic, metal dielectric cavity micropillar with DBQW regions on GaAs/(Al, Ga)As materials [43] for operation at the wavelength of 850 nm and InP materials [44] for operation at 1550 nm. For simplicity, in this work we focus on one of the two material platforms and investigate InP-based RTD systems throughout our analyses. The micropillar is coated by a dielectric cap (typically made of SiO_2) and metallic layer (typically Au or Ag), similarly to previously reported waveguide-coupled nano-LEDs [45]. A significant advantage of the semiconductor RTD epilayer design is that it can be used to realize all the required functional blocks of the proposed spiking neuromorphic optoelectronic nodes, including ultrasensitive photodetectors [46,47], high-bandwidth nonlinear behavior (including spiking responses) in the electric domain, and light emission, including both coherent (laser) and noncoherent (light emitting diodes, LEDs) operations. This brings the possibility of all-in-one monolithic integration of the required functional blocks into singular submicron scale devices. Specific epilayer designs based upon different material platforms' targeting operations at the aforementioned wavelength ranges, i.e., 1550 nm (InP) and 850 nm (GaAs), are currently being investigated toward the fabrication of the systems proposed in this work. For noncoherent signaling between nodes, the RTD-LD can also be realized using a RTD-LED sub-λ element at high (multigigahertz) speeds with very low power consumption ($<$ 1 pJ per emitted spike) [43]. It was observed that the light emission efficiency of the pillar design increases with smaller sizes, with sub-λ pillars yielding very high light-extraction efficiency [48]. RTD-powered nanolasers and light sources may also benefit from their small size in terms of improved operation speed and reduced lasing threshold [49]. In a review [2], it was stated that a minimum lateral size of hardware neurons is to be expected around 100 μm. RTD components, embedded as singular or monolothic submicron structures, have the potential to be significantly smaller, overcoming one of the key expected disadvantages (large footprint) in such systems. Unlike the superconducting and fluxonic [50] solutions,

the RTD-based optoelectronic node can be operated at room temperatures.

The synaptic links in this work are required for optical signal propagation between nodes and signal weighting (controllable optical signal attenuation). Recent advances in integrated, tuneable waveguide meshes offer chip-scale solutions for linear matrix transformations [51], which typically underpin the weighting functionality in neural networks. The micropillars can be directly coupled to waveguides by the means of heterogenous integration [52] or coupled together by means of two-photon polymerization waveguiding structures [53,54]. Signal attenuation in photonic waveguides can be realized for example by the means of balanced Mach-Zehnder interferometers, directional couplers [51] or nanoscale phase-change material (PCM) cells [55]. PCM-based synaptic cells also exhibit suitability for fully optical spike-timing-based plasticity [56]. The functionality of all-optical synaptic signal weighting can also be realized using vertical cavity semiconductor optical amplifiers [57] and synaptic interconnections can also be realized using integrated optical devices based on photorefractive III-V photonic structures on silicon [58].

III. RTD-LD → RTD-PD: THEORY AND DYNAMICS

A. Single optoelectronic node

We consider the monolithic nodes as optoelectronic circuits based on a RTD element connected to electrical and/or optical modulation [Figs. 1(b) and 1(c)]. The circuit dynamics are described by Kirchhoff laws, together with a nanolaser diode model [59–63]:

$$C\frac{dV}{dt} = I - f\,(V) - \kappa S_m(t), \tag{1}$$

$$L\frac{dI}{dt} = V_m(t) - V - RI, \tag{2}$$

$$\frac{dS}{dt} = \left(\gamma_m(N - N_0) - \frac{1}{\tau_p}\right)S + \gamma_m N + \sqrt{\gamma_m NS}\,\xi(t), \tag{3}$$

$$\frac{dN}{dt} = \frac{J + \eta I}{q_e} - (\gamma_l + \gamma_m + \gamma_{nr})N - \gamma_m(N - N_0)|E|^2. \tag{4}$$

Here, V is the voltage along the RTD, $I(t)$ is the circuit's total current, $S(t)$ is the photon number, and $N(t)$ is the carrier number; R is the circuit equivalent resistance and L is the intrinsic inductance of the circuit, while C is the parasitic capacitance of the RTD; $V_m(t)$ is the modulation voltage function. We consider two node models: (a) receiver, an O-E RTD integrated with a PD, governed by Eqs. (1) and (2), which can be driven by external optical pulses [represented as $S_m(t)$], where κ is the photodetector conversion factor translating input optical intensity into a photocurrent [42] signal; (b) master, an E-O RTD-LD node, governed by all the shown equations [Eqs. (1)–(4)] with omission of the PD term. We assume a low input optical power level (with small power variations), allowing for use of linearized sensitivity-power relation in the PD term [47] and static $f\,(V)$. Because of the reduced cavity size, the spontaneous and stimulated emission rates are modified as a result of Purcell enhancement of both the radiative processes [59]. For simplicity of analysis, the rate equation model includes only homogeneous broadening effects. The variable N_0 is the transparency carrier number, τ_p is the photon lifetime, $\gamma_m, \gamma_l, \gamma_{nr}$ are respectively the spontaneous emission rate into the lasing mode (where $\gamma_m S$ is the stimulated emission rate), radiative decay into the leaky modes, and nonradiative spontaneous emission coefficients; q_e is the electron charge and J is an input bias current injected into the LD in addition to the RTD current $I(t)$. The stochastic nature of the system is given in Eq. (3) by the term $\gamma_m N$ and the multiplicative noise $\sqrt{\gamma_m NS}\xi(t)$, where $\xi(t)$ is a time-uncorrelated white noise function. The parameters used in this work are available from the Supplemental Material [35]. The function $f\,(V)$ accounts for the nonlinear relation between the voltage applied across the RTD and the current passing through it. We use an analytical expression for $f\,(V)$ derived in Ref. [64] and detailed in the Supplemental Material [35]. The device operates at room temperature (300 K). Figure 1(b) shows the experimentally fitted $f\,(V)$ characteristic (parameters available from the Supplemental Material [35]) with a relatively narrow region of negative differential conductance embedded in between two regions of positive differential conductance, labeled as NDC, PDC I, and PDC II, respectively. The curve peak is located at $V = 609.6$ mV, with a local maximal current of 338.6 μA. At the right of the peak, the current abruptly drops from 340 to 80 μA in a span of less than 1 mV. Further rightwards, $f\,(V)$ continues to decrease, although with a much more moderate rate, until it reaches a valley at $V = 720.7$ mV and a local minimal current of 73.6 μA. Beyond this point, $f\,(V)$ increases again following a diodelike behavior.

B. Dynamical behavior

When the system [Eqs. (1), (2)] is biased in the proximity of the peak or valley of its I-V curve and injected with positive or negative voltage pulses, respectively, it behaves as an excitable system able to respond with electronic spikes. Using this functionality, numerical simulations of Eqs. (1), (2), (3), (4) are run, where a train of square negative voltage pulses V_m is used to trigger a spike in the RTD-LD optoelectronic master node [Fig. 2(a)]. Here, the RTD is biased close to the valley point at 750 mV. The period of the train is 2 ns and each pulse is 50 ps long and 100 mV deep. No optical modulation is used [i.e., $S_m(t) = 0$]. In total 50 simulations are run over 10 periods

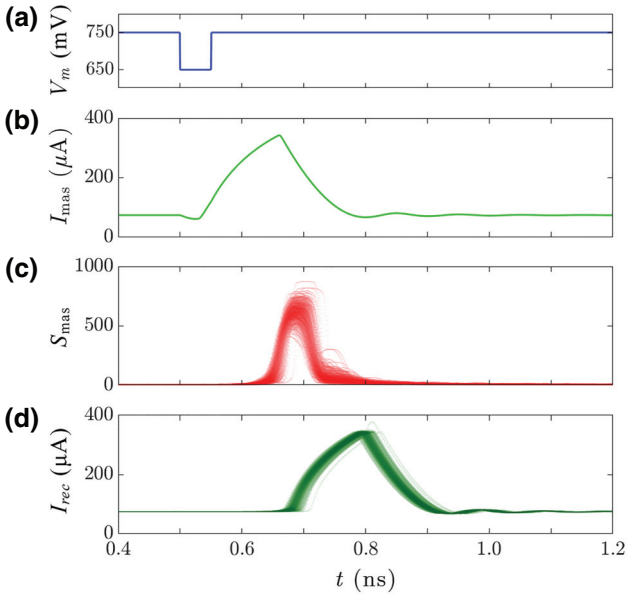

FIG. 2. Steps in 500 responses of the master-receiver optoelectronic system to the same input square pulse. The RTD elements and LDs are biased at $V_0 = 750$ mV and $J = 210$ μA, respectively. (a) Square voltage perturbation injected into the master RTD element. (b) Master RTD electronic pulse response. (c) Master LD optical pulse response. (d) Receiver RTD electronic (current) pulse response.

(thus, a total of 500 pulses are injected). The RTD responds with upward current pulses [Fig. 2(b)], each about 275 ps long and reaching a peak of 342 μA. The response delay is roughly 25 ps and the rest value of the signal is 74 μA. Such pulse elicits a weak response when injected into the LD because its peak value only slightly surpasses the LD threshold current for a very brief time. This is why the additional input bias current J is necessary. When the LD is biased at $J = 210$ μA, the total current injected $J + I_{\mathrm{mas}}(t)$ has a rest value of 284 μA and a peak value of 552 μA, well below and well above the threshold current, respectively. In consequence, the LD remains inactive most of the time and emits a pulse in response to each current pulse [Fig. 2(c)]. The optical pulse is shorter, with a duration of 40–60 ps [with temporal fluctuations due to the white noise term in Eq. (3)] because the LD takes a relatively long time to respond to an above-threshold current, while it quickly stops emitting as the current descends under the threshold. This results in the optical pulse being shortened and the response latency increased up to about 75 ps. This phenomenon is typical in systems that exhibit transcritical bifurcations and is known as *critical slowing down* [65–68]. The estimate for RTD-LD power consumption is based on the idle state current (284 μA), multiplied by the idle voltage bias (750 mV for valley point), resulting in 213 μW. This is inclusive of the additional J term that sets the subthreshold operation current of the laser. The spiking itself, due to its very short temporal timescales, will require a small amount of additional power. Assuming for the spiking event a peak current of 552 μA and the same voltage value of 750 mV gives a power of 414 μW during an approximate time of 100 ps [based on the pulse shape from Fig. 2(b)] with a maximum spiking repetition rate interval of approximately 420 ps. Hence, the upper bound on power consumption in the system can be taken as a temporally weighted average of the *spike* (100 ps) and *idle* (320 ps) states, resulting in 261 μW. Higher firing sparsity (lower spiking rate) with an increased interspike timing interval will reduce the total power consumption. With an upper bound on the spike firing repetition rate of 420 ps, the total energy consumption per spike can reach values as low as 110 fJ. We also note that peak and valley voltages in RTDs can be much smaller than 0.5 V, and that RTDs and nanolasers can be designed for operation at lower currents (10–100 μA) [59] to further reduce power consumption. In summary, the optoelectronic RTD-LD node has been demonstrated as an excitable system able to generate short optical pulses with low power consumption.

To facilitate networking, the optical pulse leaving the optoelectronic node can be used to drive a second node in a master-receiver layout. With the receiver RTD-PD circuit biased close to the valley of its I-V characteristic [$V_m(t) = V_0 = 750$ mV], the perturbation $\kappa S_{\mathrm{mas}}(t)$ is able to elicit an excitable response from the receiver RTD in the form of an excitatory current pulse similar to that produced by the master RTD [Fig. 2(d)], albeit with a fluctuating character. Therefore, the master-receiver integrated circuit is able to propagate (cascade) information by means of optical pulses. The low required values of the κ conversion factor (see the Supplemental Material [35]) used in the model demonstrate that cascaded responses require only a small portion of the optical output energy produced by upstream nodes, further increasing the prospects of larger fan-ins and fan-outs in networks.

IV. INFORMATION PROCESSING WITH RTD-BASED OPTOELECTRONIC NODES

A. Single-node 8-bit pattern recognition task

Neurons have the ability to integrate a series of input stimuli and elicit a single spike firing response. This happens due to the cumulative effect of separate input perturbations that, when combined, can exceed the neuron firing threshold intensity. A similar integrate and fire (I&F) behavior can be replicated with RTD devices.

To demonstrate this, we model the dynamical response of a single RTD-LD node driven by an AC signal V_m consisting of short negative subthreshold square pulses. In this case, the RTD is biased at a voltage $V_{\mathrm{DC}} = 730$ mV ($I_{\mathrm{DC}} = 73$ μA), which positions the device's operation point in the valley slightly to the right of the NDC

region. The LD is biased at $J = 210\ \mu$A; thus, the total current injected ($J + I_{DC}$) has a rest value of 283 μA (below the lasing threshold current). For simplicity, we do not include a receiver RTD-PD circuit, but it is assumed that a perturbation S_{mas} can be propagated to a receiver node in the form of an excitatory current pulse. To show the circuit's I&F functionality, the RTD element is driven by an AC signal consisting of 50 ps pulses of amplitude $V_{AC} = -15$ mV, separated by 50 ps. Thus, the resulting modulation signal is $V_m = V_{DC} + V_{AC}$. Figure 3(a) shows the input signal V_m (top), which consists of three pulse trains with six, seven and eight pulses, respectively, and the resulting RTD-LD output trace S_{mas} (bottom). For modulation signals containing less than eight pulses, the output remains unperturbed. However, as the number of pulses is increased to eight, their combined effect triggers a firing event in the RTD element, eliciting in turn a spike in the LD output. This I&F behavior can be exploited to perform

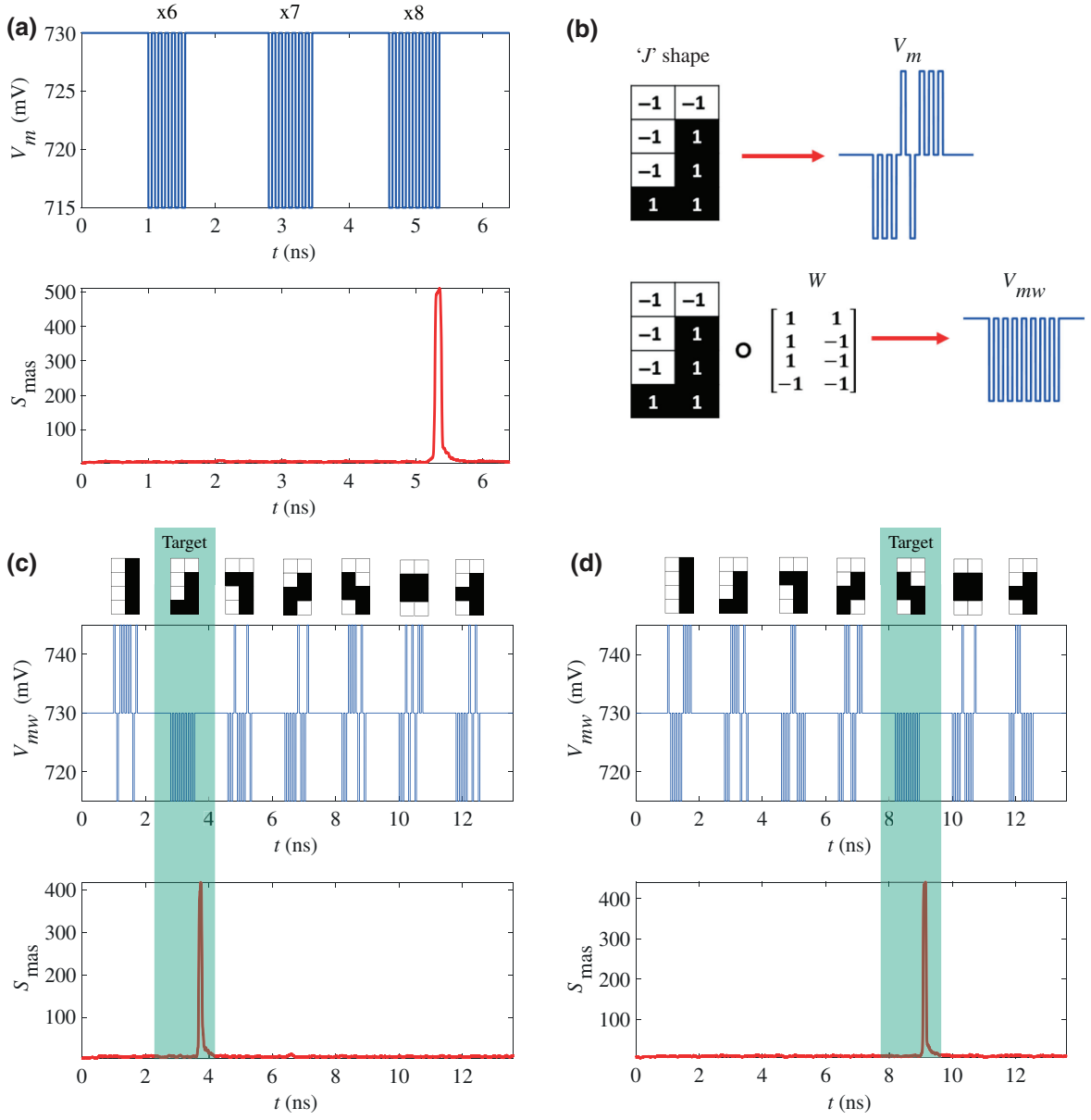

FIG. 3. (a) RTD-LD response to an AC modulation signal containing three sets of negative square signals with six, seven, and eight negative pulses, respectively (top), and the corresponding LD output trace (bottom). (b) Example of a Tetris J block represented by a 4×2 grid and corresponding serialized signal V_m (top). The J block is weighted offline by elementwise multiplication with a matrix W converting V_m to V_{mw} (bottom). (c)–(d) Simulation of pattern recognition tasks, where W is chosen to target the J (c) and S block (d), respectively. The corresponding driving signal V_{mw} is shown (top) accompanied by the LD output trace (bottom). The LD outputs have been smoothed by taking a moving average $t_{MA} = 0.1$ ns to approximate the effect of the response time of the photodetector and to ease the visualization.

an 8-bit pattern recognition task by a single RTD-LD node at very high speed, as demonstrated in Figs. 3(b)–3(d).

In this example, seven different 8-bit patterns, representing Tetris-like blocks, are mapped onto a 4 by 2 grid with individual values of 1 and −1 (representing black and white color pixels, respectively). The corresponding pattern is described by V_m as a serialized 8-bit signal [top of Fig. 3(b)]. Subsequently, each pattern is multiplied offline by an array of weights W associated with a target Tetris piece. In the example shown in Fig. 3(b), the elementwise multiplication between the J-block pattern and $W = [-1, -1, -1, 1, -1, 1, 1, 1]$ converts the input to a serialized all-negative 8-bit signal V_{mw}. For the simulation, V_{mw} included seven patterns separated by 1 ns. Each bit had an activation time of 50 ps with an amplitude $V_{AC} = \pm 15$ mV, separated by 50 ps. Two examples of a weighted modulation signal V_{mw}, used to recognize a J-shaped and S-shaped target pieces, respectively, along with their corresponding LD (S_{mas}) output traces, are shown in Figs. 3(c) and 3(d). As highlighted by the shaded green boxes, the RTD-powered node is able to successfully integrate eight pulses (bits) and fire an optical spike, thus being able to recognize the desired target piece in each case.

B. Image edge detection task using subthreshold pulse integration

We further demonstrate the possibility of using a single RTD-LD node to perform image edge detection. For this task, we utilize a binary image M of size $n \times n$ [Fig. 4(a)], where black and white pixels are assigned the values 1 or −1, respectively. In the preprocessing phase, an elementwise product between a 3×3 matrix kernel K and sections of the binary image M_h is performed offline:

$$P = K \circ M_h = \begin{bmatrix} 1 & 0 & 1 \\ 0 & -3 & 0 \\ 1 & 0 & 1 \end{bmatrix} \circ \begin{bmatrix} M_{i,j} & M_{i,j+1} & M_{i,j+2} \\ M_{i+1,j} & M_{i+1,j+1} & M_{i+1,j+2} \\ M_{i+2,j} & M_{i+2,j+1} & M_{i+2,j+2} \end{bmatrix}. \quad (5)$$

Here i and j are the indices of the individual pixels in M_h. The resulting matrix P is serialized as a 9-bit pattern, where each bit is assigned a 50 ps activation pulse and a 50 ps separation for a total of 100 ps per bit. Each pulse is assigned an amplitude $V_{AC} = \pm 16\ \text{mV} * P_{k,l}$, where k and l are the indices of individual matrix elements in P. The serialized bits are sorted such that their amplitude is rearranged in descending order. This ensures that all negative pulses are integrated consecutively to elicit a firing response. The resulting 9-bit modulation signal (V_m) is used as the electrical input for the RTD-LD node. The process described above is repeated for each row of M, taking steps of 1 pixel. Finally, the output of the RTD-LD device is used to reconstruct a binary image Q, where pixels are assigned a value of 1 when the laser output trace exhibits a spike and −1 otherwise.

An example of an 11×11 binary image, used to demonstrate edge detection operation, is shown in Fig. 4(b). Each row of M is described by a modulation signal V_m, like shown in the top plot of Fig. 4(c), consisting of nine patterns with a duration of 100×9 ps each and temporally separated by 750 ps to account for the time required for the LD output to return to zero. For the simulation, the RTD is biased at the valley $V_{DC} = 730$ mV. The corresponding S_{mas} time trace, displayed in the bottom plot of Fig. 4(c), shows two spikes of the LD output (pixels 4 and 6) as a result of the I&F response of the RTD [red box in Figs. 4(b) and 4(d)]. Figure 4(d) shows a color plot of the LD output traces for each row of M, where the high values of S_{mas} correspond to a detected edge. A binary image Q, reconstructed from the RTD-LD output, is shown in Fig. 4(e). It can be observed that, following an offline elementwise multiplication operation with a single 3 by 3 kernel, the RTD-LD node is able to consistently detect all edges of M, regardless of their orientation. We further show the capability of a RTD-LD to consistently detect all edge features, by using a 50×50 pixel binary image of the logo of the Institute of Photonics (IoP) at the University of Strathclyde [Fig. 4(f)]. The reconstructed image in Fig. 4(g) shows that the RTD-LD node is able to detect all edges with a 99.7% accuracy. These results represent example of functional tasks that can be performed by exploiting the I&F response of a RTD-based spiking node.

C. Feedforward network of optoelectronic nodes

Since the information processing capability of an artificial neural network typically grows with increasing network complexity, demonstrating networking performance with multiple optoelectronic spiking nodes is of key importance. Here, we numerically investigate the operation of a spiking variation on the single layer, feedforward perceptron model with all-to-one layout. Such network processes input spike-represented data by weighting the signal from each upstream node and summing all the weighted inputs on the downstream node, which fires a spike if the weighted input sum exceeds the firing threshold. In the demonstrated model, the spatiotemporal patterns of input superthreshold stimuli are injected into the first layer of neurons (pre-nodes), where each stimuli results in a guaranteed optical spiking outcome from the corresponding pre-node. The optical spiking signals from the pre-nodes are weighted by attenuating them (multiplying their intensity by a given factor w_n in the numerical model). During the network learning phase, a guiding signal carries the data labels alongside each pattern, marking it as wanted (true) or unwanted (false) via a change in amplitude. The downstream post-node performs the temporal integration of the upstream inputs and fires a spike if the voltage of

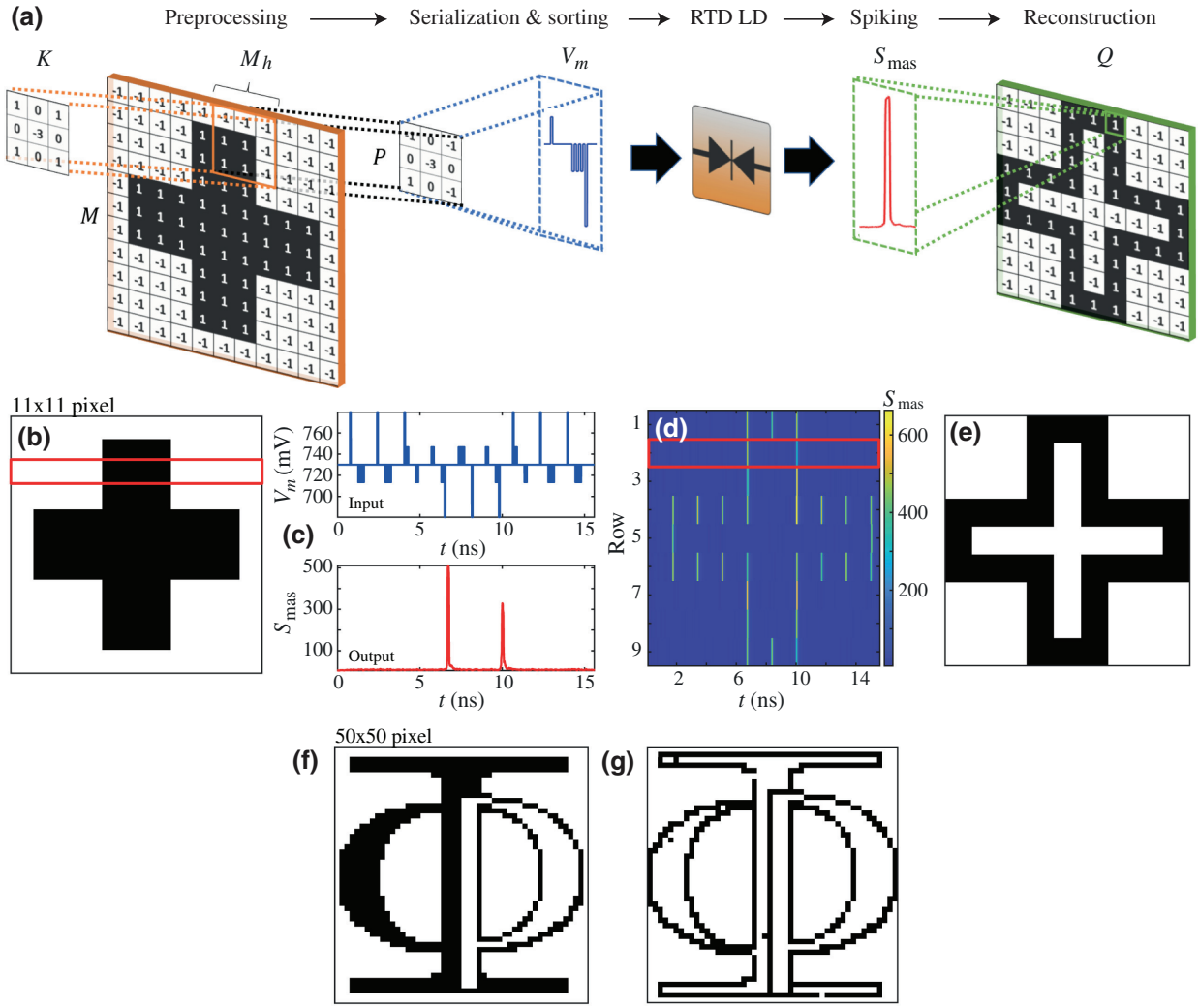

FIG. 4. (a) Steps followed to perform an edge detection task by a RTD-LD device. The process consists of four main steps: offline multiplication of a binary image M and kernel K, serialization and sorting of the 9-bit pattern to generate a modulation signal V_m, simulation of the RTD-LD response to V_m, and reconstruction of the LD output to a binary image Q. (b) The 11×11 pixel binary image used for the edge detection task, where pixels are assigned values of 1 (black) or -1 (white). (c) Example of the modulation signal used as input to drive the RTD (top) and corresponding LD output trace (bottom). (d) Color plot showing the complete LD output series used for the edge detection of M [the red box corresponds to the S_{mas} output plot shown in (c)]. (e) Reconstruction of the LD output trace into a binary image Q. (f) The 50×50 binary image of Strathclyde's Institute of Photonics (IoP) logo. (g) Reconstructed image after a single RTD-LD edge detection task.

spiking threshold is surpassed (I&F operation). A diagram of the network is depicted in Fig. 5(a), showing how different patterns (consisting of spikes, in blue) may result in activation of spikes and illustrating the dependence of weights on the output of the downstream node.

In particular, the investigated network consists of five layer-1 RTD-LD nodes (PREs, biased in the valley in PDR II, $V_{\text{DC}} = 770$ mV), whose output optical signals are propagated through unidirectional, feedforward links (each with weight w_i) to a single, layer-2 PD-RTD (post-node) node biased in the valley (in PDR II). In PD-RTD, the PD is current coupled into the spiking RTD element (with the PD conversion factor κ), directly converting the incoming optical intensity into the electrical domain and resulting in activation of an electronic spiking signal. In the PREs, we utilize superthreshold input trigger pulses of length $t_{\text{pulse}} = 80$ ps, resulting in excitatory (increasing intensity) optical pulses. Since the output current of a PD at a given time directly depends on the input light intensity and temporal distance from previous optical spikes, only certain weighted pulse patterns may result in sufficiently strong current modulation, activating a spike in the downstream node. That is the working principle of the network model for input spatiotemporal spike-pattern recognition. Visualization of the pattern recognition in the network is shown in Fig. 5(b). In this network, the temporal separation between

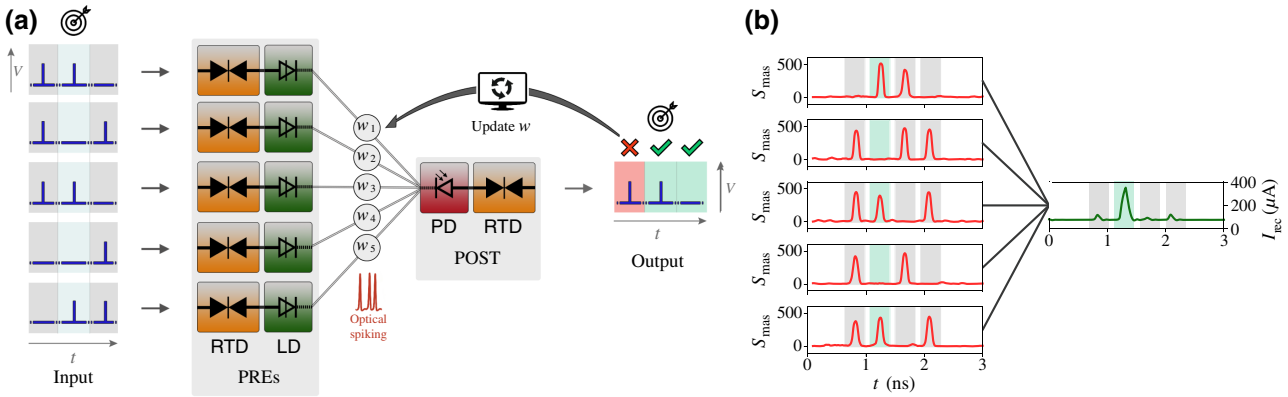

FIG. 5. (a) Network architecture diagram, illustrating how patterns of input electronic pulses (in blue) enter the RTD-LD nodes and are propagated as optical signals to the downstream node using a weighted connection. The output state of the downstream node is compared to the label, and if there is a mismatch between the label and output state, the weights are updated. Desired pattern is highlighted with the target icon. (b) Visualization of inference in a 5-to-1 feedforward network numerical model. The guiding signals representing pattern labels are visualized as background shading (green for "true," gray for "false"). Only a particular spatial pattern ([1 0 1 0 1], green) results in the firing of an electric spike of the downstream RTD-PD node (green current trace). The red timetrace represents a simple moving average of the LD output optical signal over $t_{MA} = 100$ ps.

each 5-bit input pattern is set to 420 ps, corresponding to a full network processing capacity of 11.9 Gbit/s.

D. Networks: supervised learning method for spatiotemporal pattern recognition

Training algorithms are fundamental for useful utilization of artificial neural networks (ANNs). However, training methods for spiking neural networks (SNNs) differ from those used for conventional ANNs, which are typically based on backpropagation [6]. SNNs can be trained using either biologically plausible local learning rules [e.g., spike-timing-dependent plasticity (STDP), long-term potentiation] or using other specially designed algorithms such as ReSuMe [69], resilient-back-propagation-inspired supervised learning [70], and SuperSpike [71], among others. In this work, we introduce an offline supervised learning rule, following the approach introduced in Ref. [72] for training memristor-based neural networks. However, in contrast to Ref. [72], our system propagates information using optical spike trains, allowing us to fully benefit from the advantages of optical signaling (e.g., high-bandwidth, low-loss waveguiding, noninteracting signals, etc.). Data processing in our network follows two typical phases: (a) the *training* phase and (b) the *inference* phase. During the training phase, labeled patterns are processed by the network. By comparing the output state of the network with the label, appropriate adjustments are made to the network weight matrix. The learning phase consists of multiple epochs, and progresses until the weights stabilize. During a single epoch, the dynamical evolution of all the RTD-based nodes in the network is numerically evaluated. The use of teacher signals (which carry the label of the pattern) allows for processing of multiple patterns in a single epoch. In the learning phase, three independent patterns are processed per single epoch of $t = 5$ ns.

Figure 6 shows the learning process. The target input is a 5-bit spatial pattern, either [0 1 0 1 0] [Fig. 6(a)] or [1 0 1 0 1] [Fig. 6(b)], and the network is initiated with all weights set to an initial value $w = 0.4$. We want to note here that the weights depend on the current conversion factor κ of the PD, which is selected in this demonstration to bound the weights in the usual interval [0,1]. During each learning epoch, three random patterns are picked, with a probability $P_t = 0.25$ of picking the target and $P_f = 0.75$ of picking any other pattern. Figure 6 shows the evolution of the weights during each learning step. A green background represents *true positive*, *true negative* outcomes, while red represents *false positive*, *false negative* outcomes. For either *true* output state, no weights are adjusted during the learning step. For the *false positive* output state, the weights that contributed to the firing are weakened, with Δw being a function of the post-node to pre-node spike timing separation. The closer the pre-node's spike is to activation of a *false positive* post-node spike, the higher the depotentiation (weakening) effect. This is a supervised variation on the STDP learning protocol, a specific kind of Hebbian learning approach that is believed to constitute part of the learning process in biological neural networks. A simple rational function is selected for the weight adjustment:

$$\Delta w_n = \frac{a}{b|\Delta T_n| + c} + d. \tag{6}$$

Here

$$\Delta T_n = T_{\mathrm{POST}} - T_{\mathrm{PRE},n} \tag{7}$$

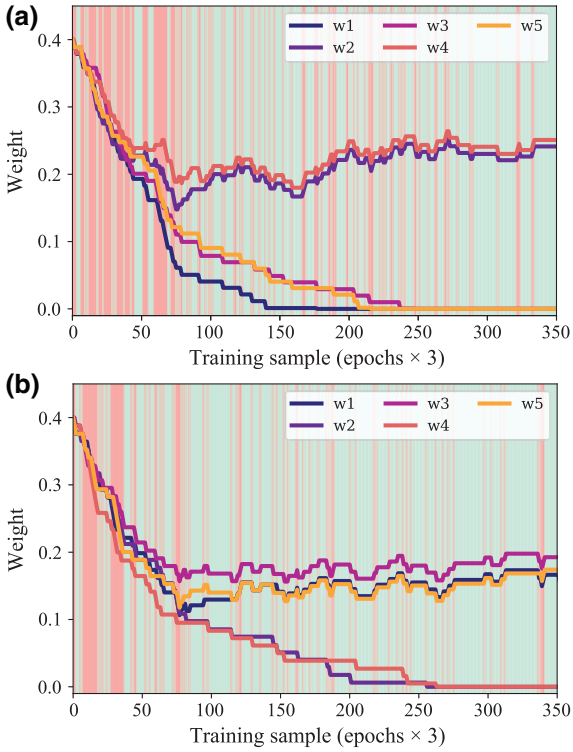

FIG. 6. Demonstration of the supervised learning process for two different spatial patterns with varying numbers of active bits: (a) [0 1 0 1 0] and (b) [1 0 1 0 1]. As the system is used to process labeled patterns in each epoch, the weights are adjusted using the local learning rule, strengthening connections that produced false negative results and weakening links that produced false positive results. The background color shows the network state (true or false) during each step.

represents the time interval between the spikes from the post-node and the pre-node n, $a = 9.35 \times 10^{-3}$, $b = 5 \times 10^{9}$, $c = 0.8$, $d = 1.5 \times 10^{-3}$. The numerical coefficients

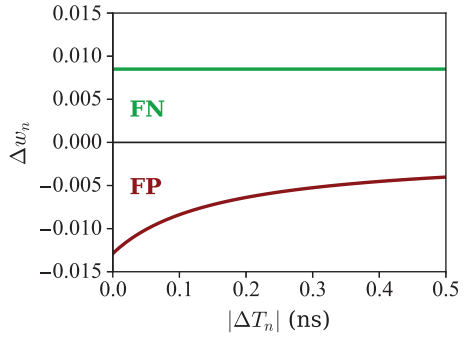

FIG. 7. Weight adjustment factor Δw_n as a function of the spiking interval $|\Delta T_n|$ between post-node and pre-node. For false negatives (FNs, in green), the weight adjustment is a constant fixed value. For false positives (FPs), the weight adjustment magnitude is a function of $|\Delta T_n|$, with closer spikes yielding stronger depotentiation.

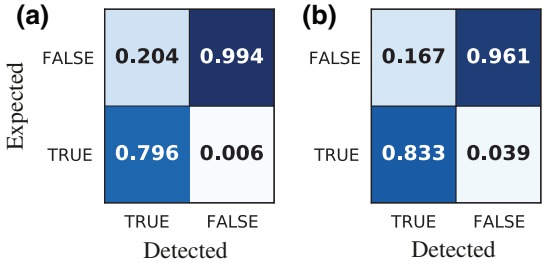

FIG. 8. Confusion matrices for (a) for inference of pattern [0 1 0 1 0] against all other patterns with two ON bits ($n = 10$ different patterns, 540 total inference steps); (b) for inference of pattern [1 0 1 0 1] against all other patterns with three ON bits ($n = 10$ different patterns, 540 total inference steps).

in the rational function are selected based on observed timings between spikes in the post- and pre-nodes and the corresponding desired weight adjustments. Weight adjustment factors as a function of the spike separation time can be seen in Fig. 7.

As the training process proceeds, the occurrence of false outcomes becomes more and more rare. For both tested patterns, the system reaches a stable weight setting in approximately 300 patterns (100 epochs). This network implementation utilizes only positive weight values, making the solution physically feasible. After the training phase, the network can perform inference for recognition of the selected spatiotemporal 5-bit pattern. We tested all patterns with an equal number of active bits against a single desired target pattern: [0 1 0 1 0] in one measurement and [1 0 1 0 1] in the other. When testing inference accuracy for [0 1 0 1 0] against all patterns with $n_{\text{on}} = 2$ active bits, the total true response accuracy (with 540 inferred patterns) is 97.4%. Inferring the pattern [1 0 1 0 1] against all patterns with same number of *on* bits ($n_{\text{on}} = 3$) in 540 inference steps yields a total true response accuracy of 94.8%. The confusion matrices for both of these inference procedures are shown in Fig. 8.

V. CONCLUSIONS

In this work, we introduce a spiking, nano-optoelectronic neuromorphic node based on a DBQW-based resonant tunneling diode exhibiting regions of NDC, enabling neuronlike electronic spiking responses at over gigahertz rates. The nodes consist of highly nonlinear, high-bandwidth RTD elements coupled to either a photodetector or a nanoscale laser to enable the reception and transmission of optical spikes, respectively. This architecture offers desirable properties, including low footprint, operation with < 100 ps input signals, and low-energy requirements (operation with millivolt trigger pulse amplitudes and energies of <pJ/spike). We investigate

and analyze the dynamical behavior of the proposed spike-based neuromorphic optoelectronic system and discuss feasible hardware implementations of individual nodes as well as architectures with nodes in interconnected networks.

We also numerically demonstrate functional information processing tasks, including 8-bit pattern recognition and image feature (edge) detection at over 10 Gbit/s rates (using 50-ps-long input signals). Finally, we demonstrate network operation, investigating a 5-to-1 feedforward spiking neural network architecture. Using physical models for each node, we demonstrate that the numerically implemented network can be used to classify spatial 5-bit pulse patterns encoded in time, and we propose a supervised learning scheme that employs a spike-timing-dependent learning rule. During the inference phase, we demonstrate 94%+ accuracy for spatiotemporal pulse pattern recognition. These reported results represent a comprehensive theoretical demonstration of RTD-based, optoelectronic, spike-based information processing and deliver successful operation in key tasks (pattern recognition, image edge detection) by utilizing either a single device or multiple interconnected devices in the form of a photonic spiking neural network.

Future work will focus on fabrication and characterization of the monolithically cointegrated RTD-PD and RTD-LD nodes and their implementation into on-chip networks. Some of the challenges ahead include the selection and implementation of optimal solutions for integrated interlinks with controllable attenuation, light coupling, and fan-in and fan-out. For the desirable operation of on-chip networks with a higher number ($\gtrsim 5$) of RTD-based artificial optoelectronic neurons, a dedicated electronic biasing circuitry will also be required to permit adaptive voltage bias tuning for each individual node. The achieved inference accuracy of approximately 94% could be further improved by, e.g., increasing the number of training process epochs. Simultaneously, since more complex and multilayer artificial neural networks typically offer better computational capability, recurrent connections and multiple (hidden) network layers will also be investigated in the future with our RTD-based approach, including extension of the presented spike-timing-based learning rule toward deep spiking networks.

ACKNOWLEDGMENTS

The authors acknowledge funding support from the European Commission (Grant No. 828841 ChipAI-H2020-FETOPEN-2018–2020), the UKRI Turing AI Acceleration Fellowships Programme (Grant No. EP/V025198/1), and the Office of Naval Research Global (Grant No. ONRGNICOPN62909-18-1-2027). The authors would like to thank Mr Martin Kot'átko for providing the three-dimensional graphical visualization of the system.

[1] E. Callaway, It will change everything': DeepMind's AI makes gigantic leap in solving protein structures, Nature **588**, 203 (2020).
[2] D. Marković, A. Mizrahi, D. Querlioz, and J. Grollier, Physics for neuromorphic computing, Nat. Rev. Phys. **2**, 499 (2020).
[3] M. V. DeBole *et al.*, TrueNorth: Accelerating from zero to 64 million neurons in 10 years, Computer **52**, 20 (2019).
[4] M. Davies *et al.*, Loihi: A neuromorphic manycore processor with on-chip learning, IEEE Micro **38**, 82 (2018).
[5] P. A. Merolla, J. V. Arthur, R. Alvarez-Icaza, A. S. Cassidy, J. Sawada, F. Akopyan, B. L. Jackson, N. Imam, C. Guo, Y. Nakamura, B. Brezzo, I. Vo, S. K. Esser, R. Appuswamy, B. Taba, A. Amir, M. D. Flickner, W. P. Risk, R. Manohar, and D. S. Modha, A million spiking-neuron integrated circuit with a scalable communication network and interface, Science **345**, 668 (2014).
[6] M. Pfeiffer and T. Pfeil, Deep learning with spiking neurons: Opportunities and challenges, Front. Neurosci. **12** (2018).
[7] J. Grollier, D. Querlioz, K. Y. Camsari, K. Everschor-Sitte, S. Fukami, and M. D. Stiles, Neuromorphic spintronics, Nat. Electron. **3**, 360 (2020).
[8] B. J. Shastri, A. N. Tait, T. Ferreira de Lima, W. H. P. Pernice, H. Bhaskaran, D. C. Wright, and P. R. Prucnal, Photonics for artificial intelligence and neuromorphic computing, Nat. Photonics **15**, 102 (2021).
[9] F. P. Sunny, E. Taheri, M. Nikdast, and S. Pasricha, A survey on silicon photonics for deep learning, ACM J. Emerg. Technol. Comput. Syst. **17**, 1 (2021).
[10] J. M. Shainline, in 2018 IEEE International Conference on Rebooting Computing (ICRC) (IEEE, 2018), p. 1.
[11] D. A. B. Miller, Attojoule optoelectronics for low-energy information processing and communications, J. Lightwave Technol. **35**, 346 (2017).
[12] L. De Marinis, M. Cococcioni, P. Castoldi, and N. Andriolli, Photonic neural networks: A survey, IEEE Access **7**, 175827 (2019).
[13] J. Bueno, S. Maktoobi, L. Froehly, I. Fischer, M. Jacquot, L. Larger, and D. Brunner, Reinforcement learning in a large-scale photonic recurrent neural network, Optica **5**, 756 (2018).
[14] Y. Shen, N. C. Harris, S. Skirlo, M. Prabhu, T. Baehr-Jones, M. Hochberg, X. Sun, S. Zhao, H. Larochelle, D. Englund, and M. Soljačić, Deep learning with coherent nanophotonic circuits, Nat. Photonics **11**, 441 (2017).
[15] J. Feldmann, N. Youngblood, M. Karpov, H. Gehring, X. Li, M. Stappers, M. Le Gallo, X. Fu, A. Lukashchuk, A. S. Raja, J. Liu, D. C. Wright, A. Sebastian, T. J. Kippenberg, W. H. P. Pernice, and H. Bhaskaran, Parallel convolutional processing using an integrated photonic tensor core, Nature **589**, 52 (2021).
[16] X. Lin, Y. Rivenson, N. T. Yardimci, M. Veli, Y. Luo, M. Jarrahi, and A. Ozcan, All-optical machine learning using diffractive deep neural networks, Science **361**, 1004 (2018).
[17] Y. Luo, D. Mengu, N. T. Yardimci, Y. Rivenson, M. Veli, M. Jarrahi, and A. Ozcan, Design of task-specific optical systems using broadband diffractive neural networks, Light: Sci. Appl. **8**, 112 (2019).

[18] I. Chakraborty, G. Saha, A. Sengupta, and K. Roy, Toward fast neural computing using all-photonic phase change spiking neurons, Sci. Rep. **8**, 12980 (2018).

[19] J. Feldmann, N. Youngblood, D. C. Wright, H. Bhaskaran, and W. H. P. Pernice, All-optical spiking neurosynaptic networks with self-learning capabilities, Nature **569**, 208 (2019).

[20] F. Laporte, A. Katumba, J. Dambre, and P. Bienstman, Numerical demonstration of neuromorphic computing with photonic crystal cavities, Opt. Express **26**, 7955 (2018).

[21] J. M. Shainline, S. M. Buckley, A. N. McCaughan, J. Chiles, A. Jafari-Salim, R. P. Mirin, and S. W. Nam, Circuit designs for superconducting optoelectronic loop neurons, J. Appl. Phys. **124**, 152130 (2018).

[22] V. A. Pammi, K. Alfaro-Bittner, M. G. Clerc, and S. Barbay, Photonic computing with single and coupled spiking micropillar lasers, IEEE J. Sel. Top. Quantum Electron. **26**, 1 (2020).

[23] P. Y. Ma, B. J. Shastri, T. Ferreira de Lima, A. N. Tait, M. A. Nahmias, and P. R. Prucnal, All-optical digital-to-spike conversion using a graphene excitable laser, Opt. Express **25**, 33504 (2017).

[24] C. Mesaritakis, A. Kapsalis, A. Bogris, and D. Syvridis, Artificial neuron based on integrated semiconductor quantum dot mode-locked lasers, Sci. Rep. **6**, 39317 (2016).

[25] J. Robertson, T. Ackemann, L. F. Lester, and A. Hurtado, Externally-triggered activation and inhibition of optical pulsating regimes in quantum-dot mode-locked lasers, Sci. Rep. **8**, 12515 (2018).

[26] G. Sarantoglou, M. Skontranis, and C. Mesaritakis, All optical integrate and fire neuromorphic node based on single section quantum dot laser, IEEE J. Sel. Top. Quantum Electron. **26**, 1 (2020).

[27] J. Xiang, A. Torchy, X. Guo, and Y. Su, All-optical spiking neuron based on passive microresonator, J. Lightwave Technol. **38**, 4019 (2020).

[28] J. Robertson, M. Hejda, J. Bueno, and A. Hurtado, Ultrafast optical integration and pattern classification for neuromorphic photonics based on spiking VCSEL neurons, Sci. Rep. **10**, 6098 (2020).

[29] M. Hejda, J. Robertson, J. Bueno, and A. Hurtado, Spike-based information encoding in vertical cavity surface emitting lasers for neuromorphic photonic systems, J. Phys.: Photonics **2**, 044001 (2020).

[30] M. Hejda, J. Robertson, J. Bueno, J. A. Alanis, and A. Hurtado, Neuromorphic encoding of image pixel data into rate-coded optical spike trains with a photonic VCSEL-neuron, APL Photonics **6**, 060802 (2021).

[31] S. Xiang, Z. Ren, Y. Zhang, X. Guo, Z. Song, A. Wen, and Y. Hao, in Optical Fiber Communication Conference (OFC) 2020 (OSA, Washington, D.C., 2020), p. W3A.1.

[32] Y. Zhang, S. Xiang, X. Guo, A. Wen, and Y. Hao, The winner-take-all mechanism for all-optical systems of pattern recognition and max-pooling operation, J. Lightwave Technol., **38**, 5071 (2020).

[33] F. Selmi, R. Braive, G. Beaudoin, I. Sagnes, R. Kuszelewicz, T. Erneux, and S. Barbay, Spike latency and response properties of an excitable micropillar laser, Phys. Rev. E **94**, 042219 (2016).

[34] P. Y. Ma, B. J. Shastri, T. Ferreira de Lima, C. Huang, A. N. Tait, M. A. Nahmias, H.-T. Peng, and P. R. Prucnal, Simultaneous excitatory and inhibitory dynamics in an excitable laser, Opt. Lett. **43**, 3802 (2018).

[35] See Supplemental Material at http://link.aps.org/supplemental/10.1103/PhysRevApplied.17.024072 and Refs. [73–80] for more details on the dynamics of the RTD circuit and for device parameters used in the numerical models, with additional references describing RTD dynamics [73], excitability [74–76] and devices with spiking dynamics [77–80].

[36] J. Wang, A. Al-Khalidi, L. Wang, R. Morariu, A. Ofaire, and E. Wasige, 15-Gb/s 50-cm wireless link using a high-power compact III-V 84-GHz transmitter, IEEE Trans. Microwave Theory Techniques **66**, 4698 (2018).

[37] R. Izumi, S. Suzuki, and M. Asada, in 2017 42nd International Conference on Infrared, Millimeter, and Terahertz Waves (IRMMW-THz) (IEEE, 2017), p. 1.

[38] M. Feiginov, Frequency limitations of resonant-tunnelling diodes in Sub-THz and THz oscillators and detectors, J. Infrared Millimeter Terahertz Waves **40**, 365 (2019).

[39] I. Ortega-Piwonka, O. Piro, J. M. L. Figueiredo, B. Romeira, and J. Javaloyes, Bursting and Excitability in Neuromorphic Resonant Tunneling Diodes, Phys. Rev. Appl. **15**, 034017 (2021).

[40] B. Romeira, J. Javaloyes, C. N. Ironside, J. M. L. Figueiredo, S. Balle, and O. Piro, Excitability and optical pulse generation in semiconductor lasers driven by resonant tunneling diode photo-detectors, Opt. Express **21**, 20931 (2013).

[41] B. Romeira, R. Avó, J. Javaloyes, S. Balle, C. N. Ironside, and J. M. L. Figueiredo, Stochastic induced dynamics in neuromorphic optoelectronic oscillators, Opt. Quantum Electron. **46**, 1391 (2014).

[42] B. Romeira, J. M. L. Figueiredo, and J. Javaloyes, Delay dynamics of neuromorphic optoelectronic nanoscale resonators: Perspectives and applications, Chaos: An Interdisciplinary J. Nonlinear Sci. **27**, 114323 (2017).

[43] B. Romeira, J. M. L. Figueiredo, and J. Javaloyes, NanoLEDs for energy-efficient and gigahertz-speed spike-based sub-λ neuromorphic nanophotonic computing, Nanophotonics **9**, 4149 (2020).

[44] B. Romeira, L. Pessoa, H. Salgado, C. Ironside, and J. M. L. Figueiredo, Photo-detectors integrated with resonant tunneling diodes, Sensors **13**, 9464 (2013).

[45] V. Dolores-Calzadilla, B. Romeira, F. Pagliano, S. Birindelli, A. Higuera-Rodriguez, P. J. van Veldhoven, M. K. Smit, A. Fiore, and D. Heiss, Waveguide-coupled nanopillar metal-cavity light-emitting diodes on silicon, Nat. Commun. **8**, 14323 (2017).

[46] A. Pfenning, F. Hartmann, M. Rebello Sousa Dias, F. Langer, M. Kamp, L. K. Castelano, V. Lopez-Richard, G. E. Marques, S. Höfling, and L. Worschech, Photocurrent-voltage relation of resonant tunneling diode photodetectors, Appl. Phys. Lett. **107**, 081104 (2015).

[47] A. Pfenning, F. Hartmann, F. Langer, M. Kamp, S. Höfling, and L. Worschech, Sensitivity of resonant tunneling diode photodetectors, Nanotechnology **27**, 355202 (2016).

[48] B. Romeira, J. Borme, H. Fonseca, J. Gaspar, and J. B. Nieder, Efficient light extraction in subwavelength

GaAs/AlGaAs nanopillars for nanoscale light-emitting devices, Opt. Express **28**, 32302 (2020).
[49] B. Romeira and A. Fiore, Physical limits of NanoLEDs and nanolasers for optical communications, Proc. IEEE **108**, 735 (2020).
[50] J. M. Shainline, Fluxonic processing of photonic synapse events, IEEE J. Sel. Top. Quantum Electron. **26**, 1 (2020).
[51] D. Pérez, I. Gasulla, and J. Capmany, Programmable multifunctional integrated nanophotonics, Nanophotonics **7**, 1351 (2018).
[52] D. Jevtics, J. McPhillimy, B. J. E. Guilhabert, J. A. Alanis, H. H. Tan, C. Jagadish, M. D. Dawson, A. Hurtado, P. W. Parkinson, and M. J. Strain, Characterisation, Selection and Micro-Assembly of Nanowire Laser Systems, Nano Letters, acs.nanolett.9b05078 (2020).
[53] C. Maibohm, O. F. Silvestre, J. Borme, M. Sinou, K. Heggarty, and J. B. Nieder, Multi-beam two-photon polymerization for fast large area 3D periodic structure fabrication for bioapplications, Sci. Rep. **10**, 8740 (2020).
[54] R. M. R. Adão, B. Romeira, and J. B. Nieder, in Conference on Lasers and Electro-Optics (OSA, San Jose, California, 2021), p. ATh1R.7.
[55] A.-K. U. Michel, M. Sousa, M. Yarema, O. Yarema, V. Ovuka, N. Lassaline, V. Wood, and D. J. Norris, Optical properties of amorphous and crystalline GeTe nanoparticle thin films: A phase-change material for tunable photonics, ACS Appl. Nano Mater. **3**, 4314 (2020).
[56] Z. Cheng, C. Ríos, W. H. P. Pernice, C. D. Wright, and H. Bhaskaran, On-chip photonic synapse, Sci. Adv. **3**, e1700160 (2017).
[57] J. A. Alanis, J. Robertson, M. Hejda, and A. Hurtado, Weight adjustable photonic synapse by non-linear gain in a vertical cavity semiconductor optical amplifier, Appl. Phys. Lett. **119**, 201104 (2021).
[58] P. Stark, F. Horst, R. Dangel, J. Weiss, and B. J. Offrein, Opportunities for integrated photonic neural networks, Nanophotonics **9**, 4221 (2020).
[59] B. Romeira and A. Fiore, Purcell effect in the stimulated and spontaneous emission rates of nanoscale semiconductor lasers, IEEE J. Quantum Electron. **54**, 1 (2018).
[60] H. Yokoyama and S. D. Brorson, Rate equation analysis of microcavity lasers, J. Appl. Phys. **66**, 4801 (1989).
[61] J. Mørk and G. L. Lippi, Rate equation description of quantum noise in nanolasers with few emitters, Appl. Phys. Lett. **112**, 141103 (2018).
[62] G. Bjork and Y. Yamamoto, Analysis of semiconductor microcavity lasers using rate equations, IEEE J. Quantum Electron. **27**, 2386 (1991).
[63] P. R. Rice and H. J. Carmichael, Photon statistics of a cavity-qed laser: A comment on the laser–phase-transition analogy, Phys. Rev. A **50**, 4318 (1994).
[64] J. N. Schulman, H. J. De Los Santos, and D. H. Choi, Physics-based RTD current-voltage equation, IEEE Electron Device Lett. **17**, 220 (1996).
[65] J. R. Tredicce, G. L. Lippi, P. Mandel, B. Charasse, A. Chevalier, and B. Picqué, Critical slowing down at a bifurcation, Am. J. Phys. **72**, 799 (2004).
[66] M. Marconi, C. Métayer, A. Acquaviva, J. M. Boyer, A. Gomel, T. Quiniou, C. Masoller, M. Giudici, and J. R. Tredicce, Testing Critical Slowing Down as a Bifurcation Indicator in a Low-Dissipation Dynamical System, Phys. Rev. Lett. **125**, 134102 (2020).
[67] W. Scharpf, M. Squicciarini, D. Bromley, C. Green, J. Tredicce, and L. Narducci, Experimental observation of a delayed bifurcation at the threshold of an argon laser, Opt. Commun. **63**, 344 (1987).
[68] P. Mandel and T. Erneux, Laser Lorenz Equations with a Time-Dependent Parameter, Phys. Rev. Lett. **53**, 1818 (1984).
[69] F. Ponulak and A. Kasiński, Supervised learning in spiking neural networks with ReSuMe: Sequence learning, classification, and spike shifting, Neural Comput. **22**, 467 (2010).
[70] S. McKennoch, D. Liu, and L. G. Bushnell, in The 2006 IEEE International Joint Conference on Neural Network Proceedings (IEEE, 2006), p. 3970.
[71] F. Zenke and S. Ganguli, SuperSpike: Supervised learning in multilayer spiking neural networks, Neural Comput. **30**, 1514 (2018).
[72] W. Wang, G. Pedretti, V. Milo, R. Carboni, A. Calderoni, N. Ramaswamy, A. S. Spinelli, and D. Ielmini, Learning of spatiotemporal patterns in a spiking neural network with resistive switching synapses, Sci. Adv. **4**, eaat4752 (2018).
[73] S. Diebold, K. Nishio, Y. Nishida, J.. Kim, K. Tsuruda, T. Mukai, M. Fujita, and T. Nagatsuma, High-speed error-free wireless data transmission using a terahertz resonant tunnelling diode transmitter and receiver, Electron. Lett. **52**, 1999 (2016).
[74] A. L. Hodgkin and A. F. Huxley, A quantitative description of membrane current and its application to conduction and excitation in nerve, J. Physiol. (Lond.) **117**, 500 (1952).
[75] A. L. Hodgkin, A. F. Huxley, and B. Katz, Measurement of current-voltage relations in the membrane of the giant axon of *Loligo*, J. Physiol. (Lond.) **116**, 424 (1952).
[76] L. Kuhnert, K. I. Agladze, and V. I. Krinsky, Image processing using light-sensitive chemical waves., Nature **337**, 244 (1989).
[77] A. Samardak, A. Nogaret, N. Janson, A. Balanov, I. Farrer, and D. Ritchie, Spiking computation and stochastic amplification in a neuron-like semiconductor microstructure, J. Appl. Phys. **109**, 102408 (2011).
[78] D. Goulding, S. P. Hegarty, O. Rasskazov, S. Melnik, M. Hartnett, G. Greene, J. G. McInerney, D. Rachinskii, and G. Huyet, Excitability in a Quantum Dot Semiconductor Laser with Optical Injection, Phys. Rev. Lett. **98**, 153903 (2007).
[79] F. Selmi, R. Braive, G. Beaudoin, I. Sagnes, R. Kuszelewicz, and S. Barbay, Relative Refractory Period in an Excitable Semiconductor Laser, Phys. Rev. Lett. **112**, 183902 (2014).
[80] S. Barbay, R. Kuszelewicz, and A. M. Yacomotti, Excitability in a semiconductor laser with saturable absorber, Opt. Lett. **36**, 4476 (2011).